Available online at www.sciencedirect.com
ScienceDirect
Cement and Concrete Research 38 (2008) 699–716
Cement and Concrete Research

# Identification of residual gas-transport properties of concrete subjected to high temperatures

Matthias Zeiml [a,*], Roman Lackner [a,b], David Leithner [a], Josef Eberhardsteiner [a]

[a] *Institute for Mechanics of Materials and Structures, Vienna University of Technology, Karlsplatz 13/202, 1040 Vienna, Austria*
[b] *FG Computational Mechanics, Technical University of Munich, Arcisstr. 21, 80333 Munich, Germany*

Received 23 April 2007; accepted 10 January 2008

**Abstract**

The pore space of porous materials strongly affects both mechanical and transport properties. As regards building materials such as concrete which may be exposed to severe environmental conditions, these properties determine the service life of concrete and concrete structures. Recently, the gas permeability of concrete was identified as the key parameter controlling explosive spalling and, thus, the integrity of concrete structures under fire loading. In this paper, an experimental setup for determination of the residual permeability of concrete subjected to high temperatures is presented. Two different experimental procedures, characterized by either a constant or a decreasing pressure history at the pressurized side of the specimen, are considered. Transport properties are identified on specimens made of *in-situ* as well as *laboratory-cast* concrete with or without additional polypropylene (PP) fibers after cooling from high temperature, covering a range of permeability over four orders of magnitude. The obtained results highlight the effect of additives and the production process on transport properties and, thus, on the performance of concrete under fire attack.


*Keywords:* Concrete; Durability; Permeability; Pore space; Fire; Polypropylene fibers

## 1. Introduction

The durability of concrete is strongly affected by its pore structure, the latter allowing the transport of various substances (e.g., water, vapor, aggressive agents) and therefore determining the life span of structures especially when subjected to aggressive environments (e.g., fire loading, freeze/thaw, sea water, acid attack etc.). When concrete is subjected to fire loading, the transport of water and vapor strongly affects the risk of explosive spalling, caused by the pore-pressure build-up in consequence of evaporation of capillary water [1,2]. Hereby, the permeability of concrete can be identified as the key parameter influencing the magnitude of this pore-pressure within the concrete structure.

The permeability of cement-based materials (cement mortar or concrete) can be determined by using incompressible (liquids) and/or compressible media (gases). A wide range of experimental techniques, employed either on site (*in-situ* tests) or in the laboratory (*laboratory* tests) were proposed in the literature:

(1) Using liquids as measurement medium:
- *in-situ* tests, such as the Initial Surface Absorption Test (ISAT) [3,4] or the Covercrete Absorption Test (CAT) [5];
- *laboratory* tests, such as constant-head or falling-head experiments [6,7], the beam-bending method [8,9], or tests employing dynamic pressurization [10,11];

(2) Using gases as measurement medium:
- *in-situ* tests, such as the Figg's test [3,12] or the Air Permeability of Near Surface (APNS) test [4,13];
- *laboratory* tests, such as the CEM-Bureau method [14–16], the Hassler method [15,17], or tests under changing thermal conditions [18].

* Corresponding author. Tel.: +43 1 58801 20240; fax: +43 1 58801 20298.
*E-mail address:* matthias.zeiml@tuwien.ac.at (M. Zeiml).

0008-8846/$ - see front matter © 2008 Elsevier Ltd. All rights reserved.
doi:10.1016/j.cemconres.2008.01.005

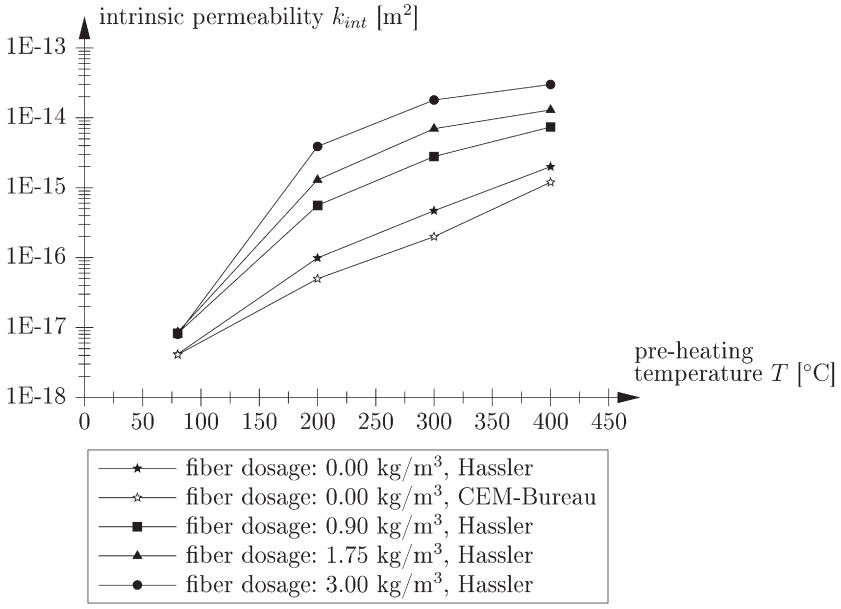


Fig. 1. Intrinsic permeability of high-performance concrete as a function of pre-heating temperature [15].

So far, the application of these test methods for determination of the influence of temperature loading on the permeability of cement-based materials was restricted to laboratory-cast specimens, e.g., the influence of the amount of polypropylene fibers (PP-fibers) on the intrinsic permeability[1] $k_{int}$ [m$^2$] for certain pre-heating temperatures was investigated in [15] (see Fig. 1). Whereas $k_{int}$ of concrete without fibers varied two orders of magnitude (caused by dehydration of the cement paste, micro-cracking due to temperature-induced stresses, etc.), a variation of $k_{int}$ of four orders of magnitude was observed for concrete with fibers within a temperature range from 80 to 400 °C. In [15], the more pronounced increase of the intrinsic permeability for concrete with PP-fibers was explained by melting of the fibers. Whereas the experiments presented in [15] were performed on pre-heated concrete specimens which were cooled down and tested at room temperature, the permeability experiments presented in [18] were conducted under changing thermal conditions (see Fig. 2). Hereby, the temperature was increased to the target temperature and the permeability test was conducted at that temperature after the temperature was kept constant for 10 h. Subsequently, the temperature was increased to the next temperature level and the same procedure was applied. The results exhibit a dent between temperatures of 100 and 200 °C. When the time span the temperature was kept constant at every temperature level was increased to 50 h, the observed dent vanished (see Fig. 2). This indicates that the increased holding time is sufficient to assure that vapor transport, which was considered to cause the aforementioned dent [18], does not disturb the permeability experiments. In [17,20], the influence of the degree of saturation on the effective permeability $k_{eff}$ (defined as $k_{int}$ for partially-saturated concrete) of cement paste and concrete was studied using the Hassler [17] and CEM-Bureau method [20]. Hereby, $k_{eff}$ decreased by two orders of magnitude for an increase of the degree of saturation from 0 to 80% (see Fig. 3). The same effect was reported in [21], where the permeability was related to the mass loss of capillary water during air drying. As reported in [20], the permeability of concrete is higher than the permeability of cement mortar. Moreover, the permeability increases with increasing water/cement-ratio, which is explained by the increased pore space that develops during curing [20].

In this paper, permeability results of in-situ as well as laboratory-cast concrete specimens with or without polypropylene (PP) fibers subjected to different pre-heating temperatures are presented, focusing on the difference in the gas-transport properties of in-situ and laboratory-cast concrete. For determination of the permeability, an experimental setup applicable to a wide range of permeability (as found in case of concrete with and without PP-fibers subjected to high temperatures) was developed. This employed setup is described in detail in the following section. Characteristics of the investigated types of concrete are given in Section 3. In Section 4, the obtained experimental results are presented. The identification of gas transport properties on the basis of the obtained results is discussed in Section 5. Finally, concluding remarks are given in Section 6.

## 2. Permeability experiments

### 2.1. Experimental setup

The experimental device used for identification of the gas-transport properties of concrete is shown in Figs. 4 and 5. Hereby, the pressure is applied via two pressure pistons with

[1] $k_{int}$ is an intrinsic parameter, describing the pore space of the material. It is independent of the medium flowing through the material. For compressible media (e.g., air or water vapor), the intrinsic permeability is defined as the permeability at infinite pressure, with $1/p=0$ [19,20].

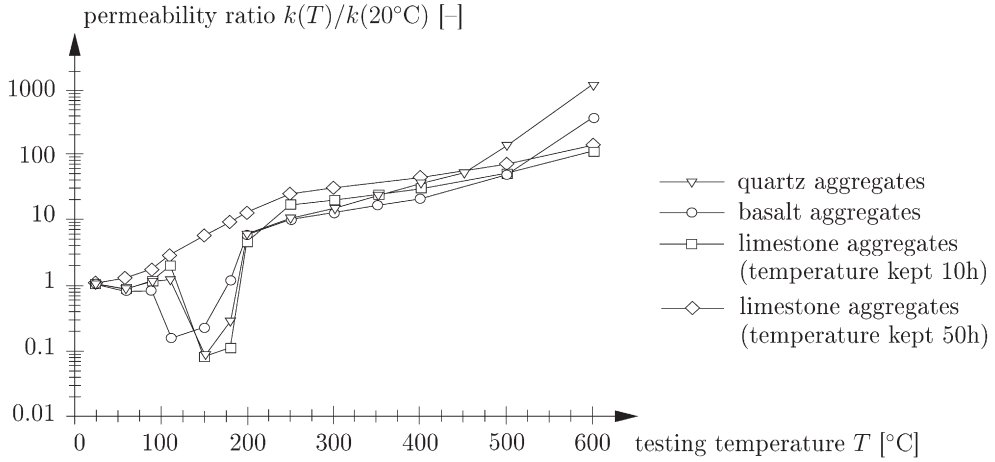


Fig. 2. Permeability of concrete (water/cement-ratio: 0.5) tested at elevated temperatures [18].

given volume. As the displacement of the pressure pistons is monitored, the amount of pressurized air provided is known. In order to cover the wide range of the permeability of concrete subjected to temperature loading, an additional air reservoir was employed, which was added to the pressurized volume in case of concrete specimens characterized by a high permeability.

With the experimental setup shown in Figs. 4 and 5, two different types of experiment may be conducted:

(1) *Decreasing-pressure experiment* (DPE): Hereby, the pressure pistons are used to increase the pressure in the system. Then, the pumping speed of the pressure pistons (controlled by $u(t)$) is adjusted in order to provide stationary air flow through the specimen at the target pressure of 8 bar (=0.8 MPa). As stationary flow is established, the air supply is closed and the decrease of pressure by air flow through the specimen is recorded as a function of time, $p_t(t)$.
(2) *Constant-pressure experiment* (CPE): Hereby, the pressure pistons (see Fig. 5) are used to maintain an almost-constant pressure at certain target pressures (ranging from 5 to 8 bar). The air flow through the specimen is determined on basis of the monitored displacement history of the pressure pistons, $u(t)$.

### 2.2. Evaluation methods

Pressure-driven flow (i.e., advection) through porous media is described by Darcy's law, giving the flux $Q$ [$m^3$/s] for the one-dimensional case as

$$Q = -k\frac{A}{\eta}\frac{dp}{dx}, \tag{1}$$

where $k$ [$m^2$] is the permeability of the porous medium, $A$ [$m^2$] is the cross-sectional area, $\eta$ [Pa s] is the dynamic viscosity of the transported fluid, and $dp/dx$ [Pa/m] is the pressure gradient. In case an incompressible fluid is advected through the porous structure, the permeability $k$ in Eq. (1) is equal to the intrinsic permeability, with $k=k_{int}$. In case of advection of compressible fluids, the so-called slip-flow phenomenon [19] is considered by

$$Q = -k\frac{A}{\eta}\frac{dp}{dx} = -k_{int}\left(1+\frac{b}{p}\right)\frac{A}{\eta}\frac{dp}{dx}, \tag{2}$$

where the pressure-dependent permeability $k$ is given by

$$k = k_{int}\left(1+\frac{b}{p}\right), \tag{3}$$

with $b$ [Pa] as the so-called slip-flow constant.

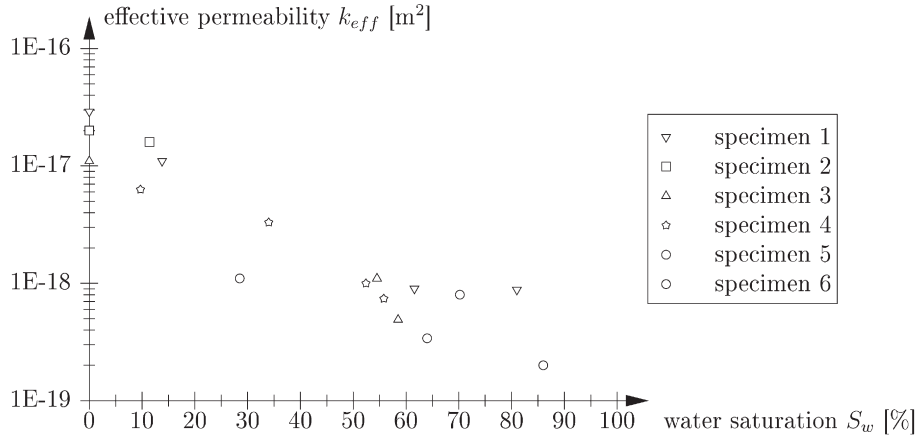


Fig. 3. Effective permeability of two-year-old normal-weight concrete (water/cement-ratio: 0.45) as a function of the water saturation [20].

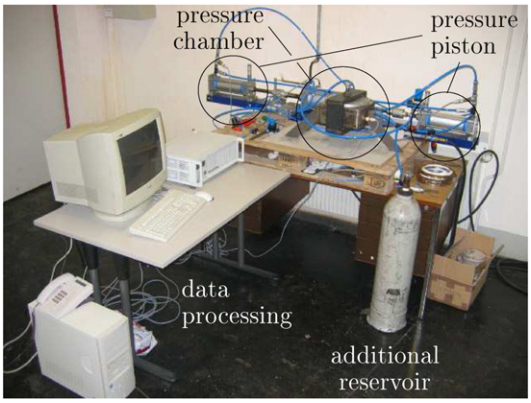


Fig. 4. Experimental setup used for permeability tests.

*2.2.1. Determination of permeability parameters $k_{int}$ and b by means of stationary analysis*

For the case of one-dimensional flow as given in the experimental setup, Eq. (2) is multiplied by pressure $p$ and, thereafter, integrated over the specimen height $H$. Accounting for $Qp$=constant [2] in case of stationary conditions yields

$$Qp\int_0^H dx = -k_{\text{int}}\frac{A}{\eta}\int_{p_t}^{p_b}(p+b)dp, \tag{5}$$

and (after evaluation of the integrals)

$$QpH = -k_{\text{int}}\frac{A}{\eta}\left[\frac{p_b^2-p_t^2}{2}+b(p_b-p_t)\right], \tag{6}$$

where $p_b=p_0\approx 1$ bar (atmospheric pressure) represents the pressure at the bottom of the specimen. During the experiments, $Q$ and $p$ at the top of the specimen (denoted as $Q_t$ and $p_t$), which are accessible through the monitored pressure history $p_t(t)$ and the history of the piston displacement $u(t)$, are determined for selected time intervals $t_1\le t\le t_2$. Within each time interval, an averaged pressure at the top of the specimen is introduced as $\bar{p}_t=[p_t(t_1)+p_t(t_2)]/2$. Considering the given values for $Qp$ at the top surface of the specimen and considering $k=k_{\text{int}}(1+b/p)$ in Eq. (6), where $p$ is set equal to $(\bar{p}_t+p_0)/2$, one gets

$$k = \frac{2H\eta}{A\left(\bar{p}_t^2-p_0^2\right)}Q_t\bar{p}_t, \tag{7}$$

where $p_t$ is replaced by $\bar{p}_t$. Eq. (7) is solved for different time intervals $t_1\le t\le t_2$ and the obtained values for the permeability $k$ are plotted as a function of $1/p$, where $p$ is again set equal to $(\bar{p}_t+p_0)/2$. The permeability parameters $k_{\text{int}}$ and $b$ are obtained from linear regression as illustrated in Fig. 6. The parameters used for determination of $k$ from the experimental data are summarized in Table 1 (additionally, $\eta=18\times10^{-6}$ Pa s). In the following, the determination of $Q_t\bar{p}_t$ required in Eq. (7) will be described for both DPE and CPE (see Appendix B for an alternative determination of $k_{\text{int}}$ and $b$).

*Determination of $Q_t\bar{p}_t$ for DPE*

During a DPE, the pressure at the top of the specimen continuously decreases in consequence of air flow through the specimen (see Fig. 7). Considering a time interval $t_1\le t\le t_2$, the amount of moles present within the pressurized volume at time $t_i$ is

$$n(t_i) = \frac{p_t(t_i)V(t_i)}{RT(t_i)}, \tag{8}$$

where $V(t_i)=V$ [$m^3$] is the constant pressurized volume (see Fig. 8 and Tables 1 and 2) and $T(t_i)=T$ [K] is the constant temperature (considering isothermal conditions). The amount of moles that pass through the specimen within time interval $t_1\le t\le t_2$, given by $n(t_1)-n(t_2)$, yields the molar flux within the considered time interval as

$$n(t_1)-n(t_2) = \frac{[p_t(t_1)-p_t(t_2)]V}{RT}\rightarrow\frac{\Delta n}{\Delta t}=\frac{\Delta p_t V}{RT}, \tag{9}$$

where $\Delta n=n(t_1)-n(t_2)$, $\Delta t=t_2-t_1$, and $\Delta p_t=p_t(t_1)-p_t(t_2)$. Rewriting Clapeyron's law for ideal gases (Eq. (4)) for the time interval $t_1\le t\le t_2$ and replacing $Q$ by $Q_t$ and $p$ by $\bar{p}_t$, one gets

$$\frac{\Delta n}{\Delta t}\approx Q_t\bar{p}_t\frac{1}{RT}. \tag{10}$$

Obviously, the quality of approximation (10) depends on the difference between $p_t(t_1)$ and $p_t(t_2)$ and improves for smaller differences, i.e., for small time intervals $t_1\le t\le t_2$. Combining Eqs. (9) and (10) gives access to $Q_t\bar{p}_t$ for the considered time interval:

$$Q_t\bar{p}_t = \frac{\Delta p_t V}{\Delta t}. \tag{11}$$

*Determination of $Q_t\bar{p}_t$ for CPE*

Within a CPE, the pumping mechanism (consisting of two pressure pistons and one driving piston) supplies air to the pressurized system (with the corresponding volume $V$ given in Table 2) in an alternate manner (see Fig. 9). One cycle of a piston consists of three phases:

(1) Phase I (backwards movement): Air flows from the gas supply to the considered pressure piston whereas the other piston supplies air to the pressurized system.
(2) Phase II (first part of piston stroke): The shift mechanism changes the pumping direction and the considered pressure piston becomes active. Since the filling pressure is chosen to be lower than the pressure in the pressurized system, the air must be compressed in Phase II before the

[2] In contrast to the volumetric flux $Q$ [$m^3$/s], which is not constant along the direction of flow in case of compressible (stationary) flow through porous media, the molar flux $dn/dt$ [mol/s] is constant. Hence, under isothermal conditions ($T$=constant), Clapeyron's law for ideal gases yields

$$nRT = Vp\rightarrow\frac{dn}{dt}RT=\frac{dV}{dt}p=Qp=\text{constant}. \tag{4}$$

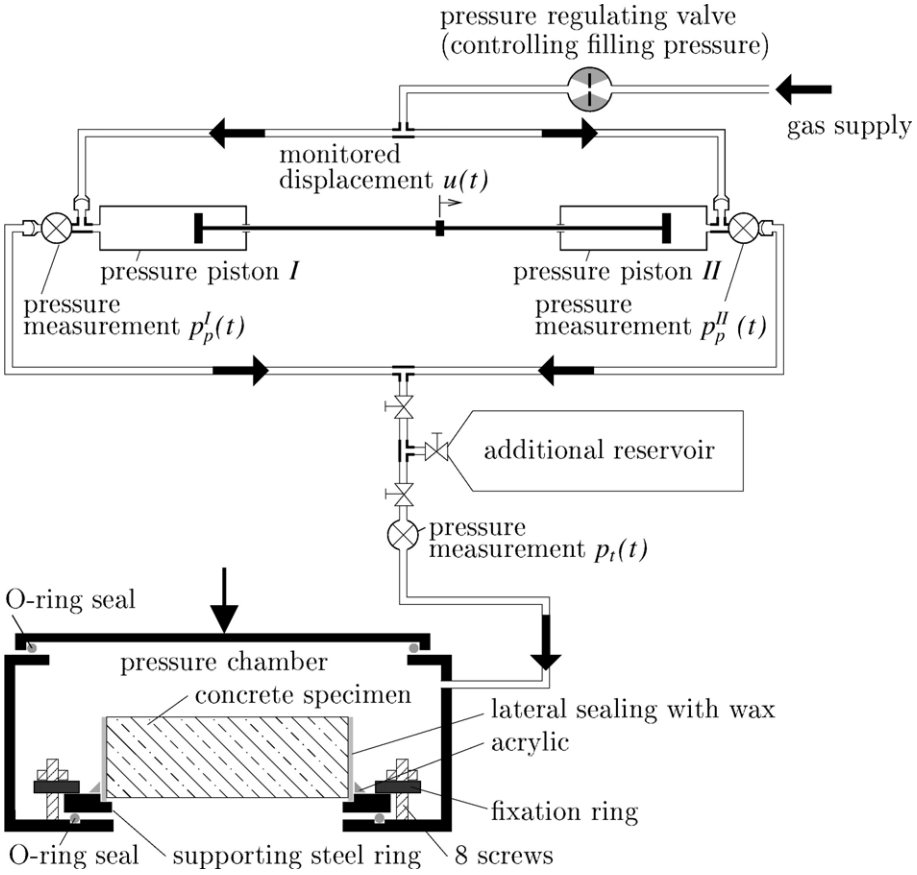


Fig. 5. Schematic illustration of experimental device used for permeability tests.

one-way valve opens and the piston supplies air to the pressurized system.

(3) Phase III (second part of piston stroke): The pressure in the piston exceeds the pressure in the pressurized system (the pressure difference needs to overcome the resistance of the one-way valve) and the piston supplies air to the pressurized system.

To determine the molar and, hence, the volumetric flux through the specimen, a mass balance is conducted over the piston stroke (Phases II and III). At the beginning of Phase II (corresponding to time instant $t_1$ in Fig. 9), the piston is filled with air at filling pressure $p_p(t_1)$ and the pressurized volume $V$ is at pressure $p_t(t_1)$, with $p_t(t_1)>p_p(t_1)$. Hence, the total amount of moles within the system (see Fig. 8 and Table 2) at beginning of Phase II can be determined as

$$t = t_1 : n(t_1) = \frac{1}{RT}\left[p_p(t_1)\left(V_p + V_{\text{rem}}\right) + p_t(t_1)V\right], \tag{12}$$

where $V_p = A_p L$, with $A_p$ [m$^2$] as the cross-sectional area of the piston and $L$ [m] as the length that the piston moves within one stroke (see Fig. 9). In Eq. (12), $V_{\text{rem}}$ [l] is the volume of the part of the piston that remains filled with air at the end of Phase III. Thus, $V_{\text{rem}}$ is not provided to the pressurized system. In Eq. (12), $V$ [l] corresponds to the pressurized volume given in Table 2 (see Fig. 8). At the end of Phase III, when the pumping direction

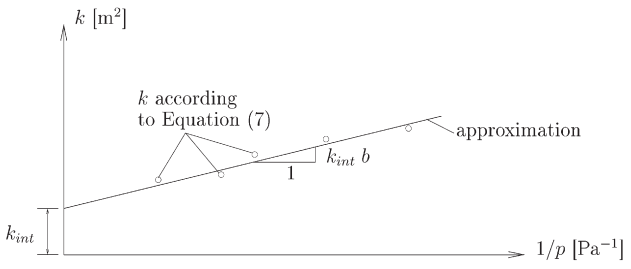


Fig. 6. Illustration of identification of permeability parameters $k_{\text{int}}$ and $b$ from regression analysis ($p$ was set equal to $(\bar{p}_t+p_0)/2$ for the respective time interval).

Table 1
Specimen dimensions and pressurized volume in experimental setup

| Parameter | In-situ concrete | Laboratory-cast concrete |
|---|---|---|
| Specimen diameter ø [m] | 0.143 | 0.150 |
| Specimen area $A$ [m$^2$] | $1.606\times10^{-2}$ | $1.767\times10^{-2}$ |
| Specimen height $H$ [m] | 0.05 | 0.05 |
| $L$ [m] | – | 0.132 |
| $A_p$ [m$^2$] | $5.027\times10^{-3}$ | $5.027\times10^{-3}$ |
| $V_{\text{chamber}}$ [l] | 4.953 | 4.942 |
| $V_{\text{pipe,1}}$ [l] | 0.0176 | 0.0176 |
| $V_{\text{pipe,2}}$ [l] | 0.0251 | 0.0144 |
| $V_{\text{reservoir}}$ [l] | 20.8 | 20.8 |
| $V_{\text{pipe,3}}$ [l] | 0.2637 | 0.2637 |
| $V_{\text{rem,I}}$ [l] | 0.1392 | 0.1392 |
| $V_{\text{rem,II}}$ [l] | 0.1078 | 0.1078 |

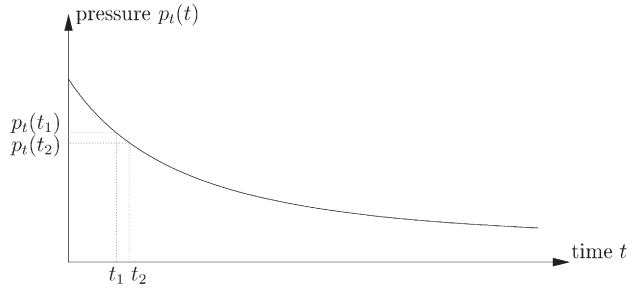


Fig. 7. Decrease of pressure $p_t$ at top of specimen recorded during DPE.

Table 2
Pressurized volume $V$ during permeability experiments

| Experiment type | Pressurized volume $V$ [l] | |
|---|---|---|
| DPE – in-situ – no reservoir | 4.97 | ($V=V_{chamber}+V_{pipe,1}$) |
| DPE – in-situ – incl. reservoir | 25.80 | ($V=V_{chamber}+V_{pipe,1}+V_{pipe,2}+V_{reservoir}$) |
| DPE – lab-cast – incl. reservoir | 25.77 | ($V=V_{chamber}+V_{pipe,1}+V_{pipe,2}+V_{reservoir}$) |
| CPE – lab-cast – incl. reservoir | 26.04 | ($V=V_{chamber}+V_{pipe,1}+V_{pipe,2}+V_{reservoir}+V_{pipe,3}$) |

is reversed (corresponding to time instant $t_2$ in Fig. 9), the pressures in the piston and the pressurized volume are almost equal, with $p_p(t_2)\approx p_t(t_2)$. Therefore, the amount of moles within the system at the end of the piston stroke is

$$t = t_2 : n(t_2) = \frac{1}{RT}\left[p_p(t_2)V_{\text{rem}} + p_t(t_2)V\right]. \tag{13}$$

Eqs. (12) and (13) yield the molar flux provided to the pressurized system within $t_1 \le t \le t_2$ as

$$\frac{\Delta n}{\Delta t} = \frac{n(t_1) - n(t_2)}{\Delta t} = \frac{1}{RT}\frac{p_p(t_1)V_p + \Delta p_p V_{\text{rem}} + \Delta p_t V}{\Delta t}, \tag{14}$$

where $\Delta p_t = p_t(t_1) - p_t(t_2) \neq 0$ even in case of CPE, caused by slight variations of the pressure in the pressurized volume. In Eq. (14), $\Delta p_p = p_p(t_1) - p_p(t_2)$ and $\Delta t = t_2 - t_1$. Considering again Clapeyron's law for ideal gases (Eq. (4)) gives $Q_t\overline{p}_t$ for the considered time interval $t_1 \le t \le t_2$ as

$$Q_t\overline{p}_t = \frac{p_p(t_1)V_p + \Delta p_p V_{\text{rem}} + \Delta p_t V}{\Delta t}, \tag{15}$$

with $\overline{p}_t = [p_t(t_1) + p_t(t_2)]/2$.

*2.2.2. Determination of permeability parameters $k_{int}$ and $b$ from DPE by means of transient analysis*

Within the identification procedure presented in the previous subsection, stationary conditions were assumed within the considered time interval $t_1 \le t \le t_2$. During the DPE, the pressure in the pressurized volume decreases, approaching the atmospheric pressure as asymptotic limit. The characteristic time

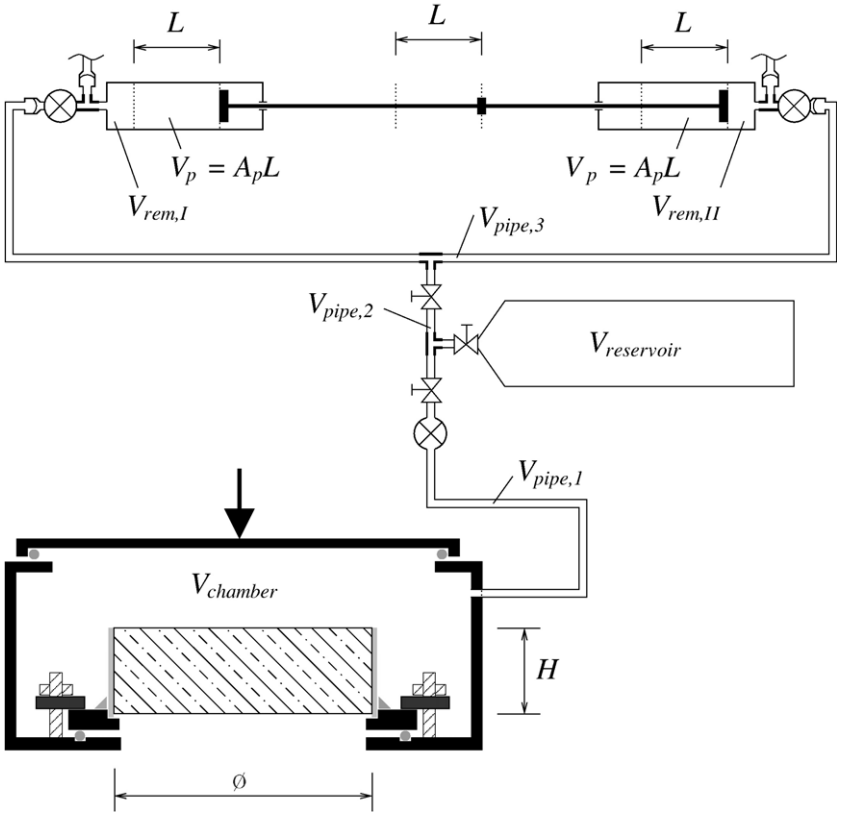


Fig. 8. Pressurized volume in experimental setup.

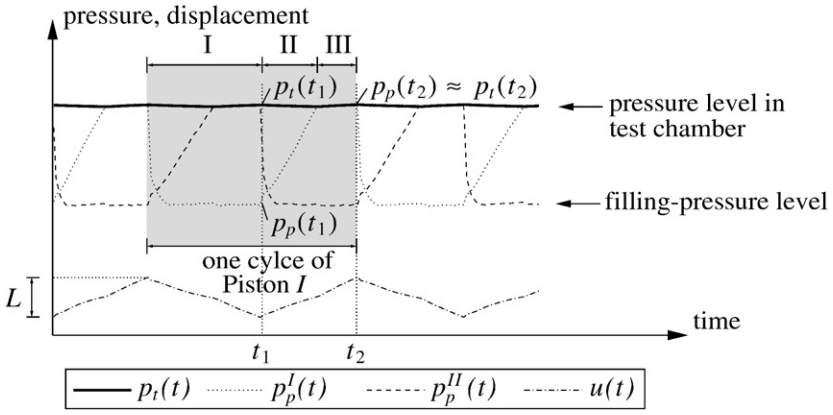


Fig. 9. Representative plot of pressure and displacement history during CPE ($p_t$: pressure at top of specimen; $p_p^I$ and $p_p^{II}$: pressure in Piston I and II, respectively; $u$: monitored piston displacement).

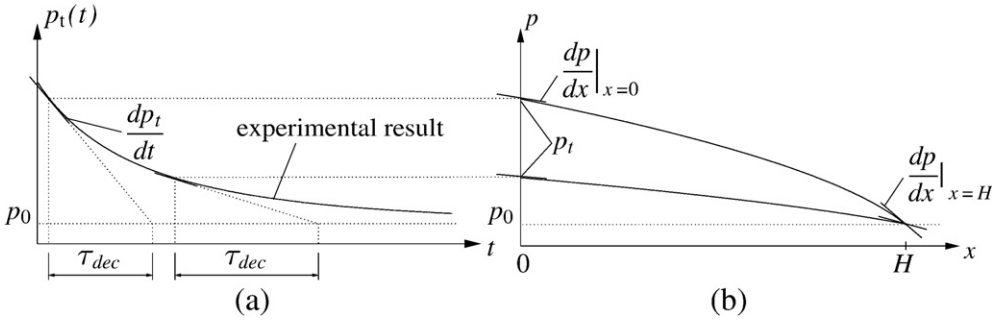


Fig. 10. (a) $\tau_{dec}$ from history of pressure $p_t$ and (b) (stationary) pressure distribution for two time instants characterized by different values of $p_t$.

associated with this pressure decrease, $\tau_{dec}$ [s], is defined by (see Fig. 10(a))

$$\tau_{dec}(t) := \frac{p_0 - p_t(t)}{dp_t/dt}, \tag{16}$$

where $dp_t/d_t$ [Pa/s] is determined from the experimentally-obtained history of pressure $p_t$.

The characteristic time associated with pressure-driven flow (advection) through the specimen, on the other hand, is given by (see, e.g., [22])

$$\tau_{adv}(t) = \frac{l}{v} = \frac{H}{-\frac{k}{\eta}\frac{dp}{dx}}, \tag{17}$$

with $l=H$ [m] as the characteristic length of advection (which is set equal to the specimen height in case of one-dimensional flow in the permeability experiments) and $v=-k/\eta \cdot dp/dx$ [m/s] as the velocity of Darcian flow (compare to Eq. (1)). Since the permeability $k$ and the pressure gradient $dp/dx$ vary over the specimen height, $\tau_{adv}$ is determined (considering a stationary pressure distribution as approximation of the real transient pressure distribution) at the upper and lower surface of the specimen (with $x=0$ and $x=$H, respectively, see Fig. 10(b)), giving the upper and lower bound of $\tau_{adv}$ for a certain time instant.

Fig. 11 illustrates the evolution of the characteristic times $\tau_{dec}$ and $\tau_{adv}$ for a selected DPE. For the calculation of $\tau_{adv}$, the permeability $k$ was determined from Eq. (3) using intrinsic permeability $k_{int}$ and slip-flow constant $b$ determined from the stationary analysis presented in Section 2.2.1. As the pressure in the pressurized system decreases in the course of the DPE (see Fig. 10(a)), both $\tau_{dec}$ and $\tau_{adv}$ increase. The ratio of the two time scales, $\tau_{dec}/\tau_{adv}$, obtained for experiments on specimens heated to different temperatures is given in Fig. 12, ranging from 1 to 5 in case the additional reservoir is not included in the pressurized volume. When the additional reservoir is included in the experiment, the time scale of pressure decrease at the

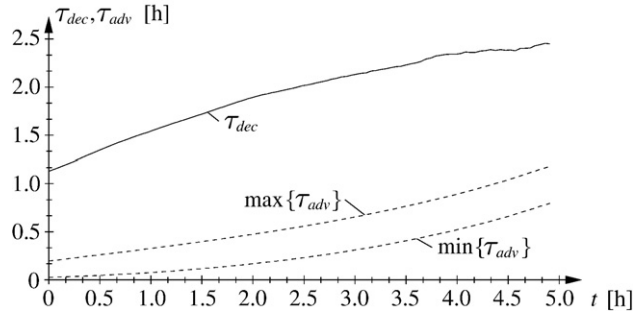


Fig. 11. Characteristic times $\tau_{dec}$ and $\tau_{adv}$ for a selected DPE (parameters used: $H=0.0495$ m; $k_{int}=1.22\times10^{-16}$ m$^2$; $b=1.34$ bar; $\eta=18\times10^{-6}$ Pa s).

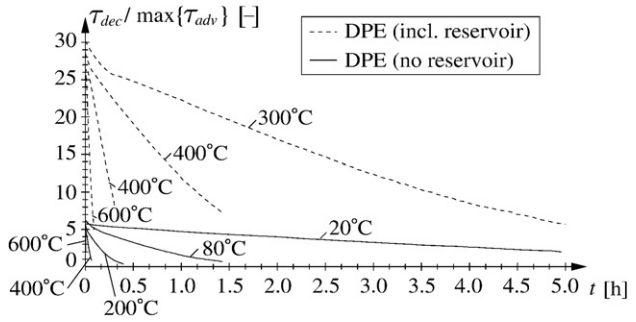


Fig. 12. $\tau_{dec}/\tau_{adv}$ obtained from testing of concrete heated to different temperature levels.

pressurized side of the specimen, $\tau_{dec}$, increases by one order of magnitude, resulting in an increase of the ratio $\tau_{dec}/\tau_{adv}$ (see Fig. 12). Based on the obtained results, $\tau_{dec}/\tau_{adv}$ was found to mainly depend on the amount of pressurized gas rather than the permeability of the tested material (controlled by temperature loading of the investigated concrete).

For $\tau_{dec}/\tau_{adv} \gg 1$, the transport through the specimen is significantly faster than the pressure decrease in the pressurized volume. Thus, for any pressure in the pressurized volume, a stationary pressure distribution is present within the specimen. For $\tau_{dec}/\tau_{adv}$ 1, on the other hand, the pressure decrease in the pressurized volume affects the pressure distribution over the specimen height, thus, making a transient analysis necessary. For this analysis, the one-dimensional mass-balance equation (see Appendix A), reading

$$n\frac{\partial p}{\partial t} - \frac{k_{int}}{\eta}\frac{\partial}{\partial x}\left[(p+b)\frac{\partial p}{\partial x}\right] = 0 \qquad (18)$$

is solved numerically for the unknown pressure $p(x,t)$. In Eq. (18), $n$ [−] represents the porosity of concrete. In the analysis, the pressurized volume is included in the numerical model (see Fig. 13), with the permeability of this part of the model as $k = 1\times10^{-3}$ m$^2$. The initial pressure distribution at $t=0$ is set equal to the stationary solution, with $p=p_t(t=0)$ at $x=x_1$ and $p=p_0$ at $x=x_{n_e+1}$ (see Table 3). For a given set of permeability parameters $k_{int}$ and $b$, the transient analysis gives access to the history of the pressure decrease at the top surface of the specimen, $p_t^{num}(t)$. This numerically-obtained history is compared with the experimental history of $p_t$ (i.e. $p_t^{exp}(t)$) for various pairs of $k_{int}$ and $b$. The pair of $k_{int}$ and $b$ that minimizes the error between the numerically and experimentally-obtained pressure history represents the set of parameters identified from the transient analysis.

Table 3
Initial and boundary conditions used within transient analysis

| | Location | Value |
|---|---|---|
| Initial conditions: | $x=x_1$ | $p=p_t(t=0)$ |
| | $x=x_{n_e+1}$ | $p=p_0$ |
| Boundary conditions: | $x=x_1$ | $Q=0$ |
| | $x=x_{n_e+1}$ | $p=p_0$ |

## 3. Materials and specimen preparation

In this paper, permeability results obtained from specimens made of concrete C25/30 (which is commonly used for tunnel linings in Austria) with/without addition of 1.5 kg/m$^3$ PP-fibers are presented. Large-scale concrete blocks of the same concrete were tested within the fire experiments described in [1]. The mix design consists of cement CEM I 42.5 R ($C_3A$-free) and fly ash as binder, various other additives, and siliceous aggregates (see Table 4).

In order to assure workability, the water/binder-ratio was varied during preparation of the laboratory-cast concrete (see Table 5). In case of in-situ concrete, the same water/binder-ratio was used for concrete with and without PP-fibers, resulting in a reduction of the slump by 2 cm. The air content of in-situ concrete with 1.5 kg/m$^3$ PP-fibers was back-calculated from the measurements of in-situ concrete without PP-fibers (see Table 5 and Appendix C).

The used PP-fibers were monofilament fibers with a diameter of approximately 18 μm and 6 mm length (see Fig. 14). Monofilament PP-fibers are extruded from the molten mass and drawn/elongated to reach the final diameter. Subsequently, they are cut to their final length [24]. The parameters of the fibers are listed in Table 6. The density of 100%-crystalline polypropylene is $\rho_c = 950$ kg/m3, whereas 100%-amorphous polypropylene has a density of $\rho_a = 850$ kg/m$^3$ [24]. Considering the density of the used PP-fibers as $\rho = 910$ kg/m$^3$ yields a crystallinity of 60%.

The in-situ specimens were obtained from the large-scale concrete blocks (1.80 m × 1.40 m × 0.50 m) used within the fire experiments described in [1], which were cast under on-site conditions. After casting, the large-scale specimens were dried at 50 °C using a heating mat placed at the center of the concrete block. Due to the rather short storage time of 15 weeks, however, the moisture content still ranged from 4.3 to 7.0 mass-% with an

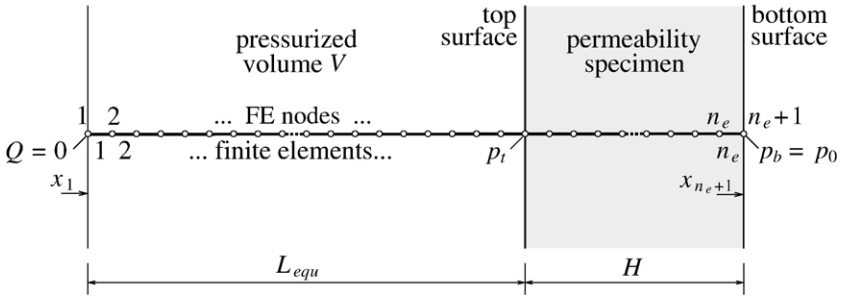


Fig. 13. Finite element (FE) model used within transient analysis ($L_{equ}$: length of part of model representing pressurized volume; $n_e$: number of finite elements).

Table 4
Mix design of concrete B30/300(56)/SA/WU/LST/FB/PB/WDI [a] [equivalent to C25/30(56)/WDI] [1,2]

| | |
|---|---|
| Cement CEM I 42.5 R ($C_3A$-free) [kg/m$^3$] | 260 |
| Additive (fly ash) [kg/m$^3$] | 60 |
| Liquefier P1 [kg/m$^3$] | 3.10 |
| Superplasticizer SP [kg/m$^3$] | 3.49 |
| Air-entrainer Ready air [kg/m$^3$] | 0.90 |
| Aggregates [b] [kg/m$^3$] | 1909 |
| Aggregate fraction 0–4 mm [mass-%] | 45 |
| Aggregate fraction 4–16 mm [mass-%] | 36 |
| Aggregate fraction 16–32 mm [mass-%] | 19 |
| Aggregate mineralogy: | |
| Quartz [mass-%] | 90 |
| Feldspar [mass-%] | 5 |
| Carbonate [mass-%] | 5 |

[a] Definitions according to [23]: SA: Sichtbeton, außen [exposed concrete, exterior]; WU: wasserundurchlässig [water-proof]; LST: stark lösender Angriff [severe leaching attack]; FB: frostbeständig [frost resistant]; PB: Pumpbeton [pumpable concrete]; WDI: wasserdichte Innenschale [water-proof tunnel lining]
[b] Aggregate content of concrete without PP-fibers, see Table 5 for details on concrete with PP-fibers.

average value of 5.5 mass-%. After the fire experiments (see Fig. 15(a)), cores 143 mm in diameter were taken from parts of the concrete blocks not affected by the fire load (see Fig. 15(b)). Thereafter, the cores were cut into discs of 50 mm height, giving the in-situ permeability specimens (see Fig. 15(c)).

The laboratory-cast specimens were produced in a similar manner. Hereby, concrete blocks with the dimensions 0.75 m × 0.30 m × 0.30 m were cast and stored under water for four weeks, together with cubes used to determine the compressive strength. The moisture content after storage ranged between 5.6 mass-% for concrete without PP-fibers and 6.4 mass-% for concrete with fibers. After curing, cores 150 mm in diameter were taken from the concrete blocks, which were then cut into 50 mm thick discs.

In-situ as well as laboratory-cast specimens were stored at similar pre-heating temperatures. In case of in-situ concrete, each specimen was subjected to two permeability tests: one without heat treatment (referred to as $T = 20$ °C in the following) or after heating to 80 °C and another test after heating to 105, 140, 200, 300, 400, or 600 °C. In case of laboratory-cast specimens, up to three experiments were performed on one specimen: one after heating to 80 °C and one or two more after heating to 105, 169, 224, 329, or 423 °C. The target temperature was reached with a heating rate of 1 °C/min. The rather slow temperature increase was chosen to avoid large temperature gradients in the specimen and, hence, severe microcracking, which would have altered the experimental results. In order to ensure that the pre-heating temperature was reached everywhere within the specimen, the samples were stored at the respective

Table 5
Parameters at mixing and 28-day strength of in-situ and laboratory-cast concrete with/without PP-fibers

| | In-situ concrete [1] | | Laboratory-cast concrete | |
|---|---|---|---|---|
| PP-fiber content [kg/m$^3$] | 0 | 1.5 | 0 | 1.5 |
| Aggregates [kg/m$^3$] | 1909 | 1874 [a] | 1909 | 1776 |
| Water [kg/m$^3$] | 157 | 157 [b] | 152.1 | 165.7 |
| Water/cement-ratio [−] | 0.60 | 0.60 | 0.59 | 0.64 |
| Water/binder-ratio [−] | 0.49 | 0.49 | 0.48 | 0.52 |
| Air content [%] | 3.5 | 4.6 [c] | 4.0 | 6.5 |
| Slump [cm] | 45.0 | 43.0 | 44.8 | 45.5 |
| Initial density [kg/m$^3$] | 2386 | 2352 | 2381 | 2263 |
| 28d-concrete density $\rho_c$ [kg/m$^3$] | 2362 | | 2355.6 | 2243.8 |
| 28d-cube compressive strength [MPa] | 52.2 | | 42.0 | 30.0 |
| 28d-bending strength [MPa] | 6.41 | 6.25 | | |

[a] Back-calculated from initial density (see Eq. (C.3) in Appendix C).
[b] Presumably same water content for both in-situ concretes.
[c] Calculated value (see Eq. (C.4) in Appendix C).

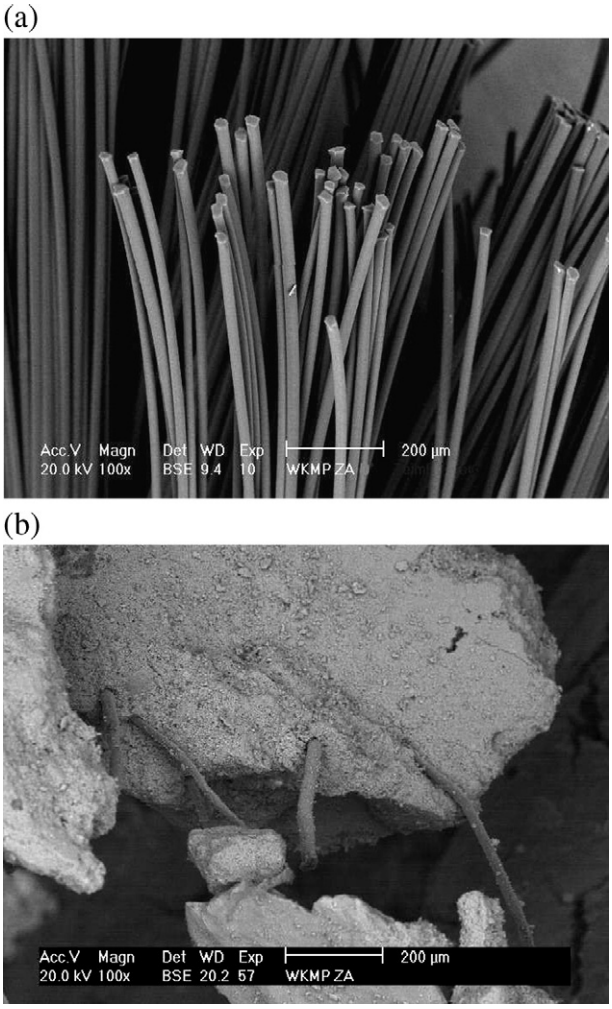


Fig. 14. Scanning-electron-microscope image showing PP-fibers (a) before casting and (b) in broken-off piece of mature concrete.

Table 6
Parameters of PP-fibers used within the concrete mix [24,25]

| Parameter | Value |
|---|---|
| Diameter [m] | $18 \times 10^{-6}$ |
| Length [m] | $6 \times 10^{-3}$ |
| Density (solid) [kg/m$^3$] | 910 |
| Density (liquid) [kg/m$^3$] | 850 |
| Crystallinity [%] | 60 |
| Melting temperature [°C] | 165 |
| Vaporization temperature [°C] | 350 |
| Tensile strength [MPa] | 400 |
| Young's modulus [MPa] | 3500–3900 |
| Poisson's ratio [−] | 0.40 |

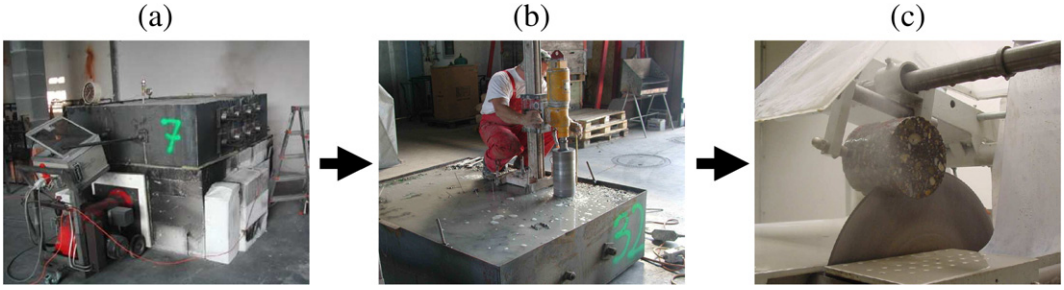


Fig. 15. Extraction of specimens for permeability testing from large-scale concrete blocks: (a) fire experiments [1]; (b) extraction of cores [1]; (c) cutting of cores into discs of 50 mm height.

target temperature for time spans up to 90 h. Thereafter, the temperature was reduced with a cooling rate of 1 °C/min.

After heat treatment, the lateral surfaces of the cylindrical specimen were sealed with wax in order to assure one-dimensional air flow through the specimen (see Fig. 16(a)). Then the specimen was placed in a steel ring (Fig. 16(b)) and the gap between specimen and ring was sealed with acrylic (see Fig. 16(c)). The specimen together with the steel ring (Fig. 16(d)) was fixed in the pressure chamber (see Figs. 4 and 16(e)) and the permeability experiment was conducted at room temperature.

## 4. Results

### 4.1. $k_{int}$ and b for in-situ concrete

Figs. 17 and 18 show the permeability parameters $k_{int}$ and $b$ as a function of temperature for in-situ concrete with 0 and 1.5 kg/m$^3$ PP-fibers, respectively. The trend for the intrinsic permeability is the same for concrete with and without PP-fibers, namely an increase of $k_{int}$ for increasing temperature. The slip-flow constant $b$, on the other hand, decreases until temperatures of 200–300 °C, and increases thereafter. In case of concrete without fibers, the results for pre-heating temperatures of 20 and 80 °C show large variations irrespective of the chosen evaluation method, which could be explained by evaporable water still present at these temperatures. This trend is also observed in case of concrete with PP-fibers, although the scatter is significantly smaller and the permeability values are higher. The obtained permeability parameters for both types of concrete show larger scatter in case the parameters were identified assuming stationary conditions.

### 4.2. $k_{int}$ and b for laboratory-cast concrete

Figs. 19 to 22 show the permeability parameters $k_{int}$ and $b$ as a function of temperature for laboratory-cast concrete with 0 and 1.5 kg/m$^3$ PP-fibers. Hereby, parameters identified from DPE and CPE are depicted separately. The same general trend as found for in-situ concrete, namely an increasing intrinsic permeability $k_{int}$ with increasing temperature, is observed for laboratory-cast concrete. As regards the slip-flow constant $b$, again a similar trend as for in-situ concrete is observed. Up to

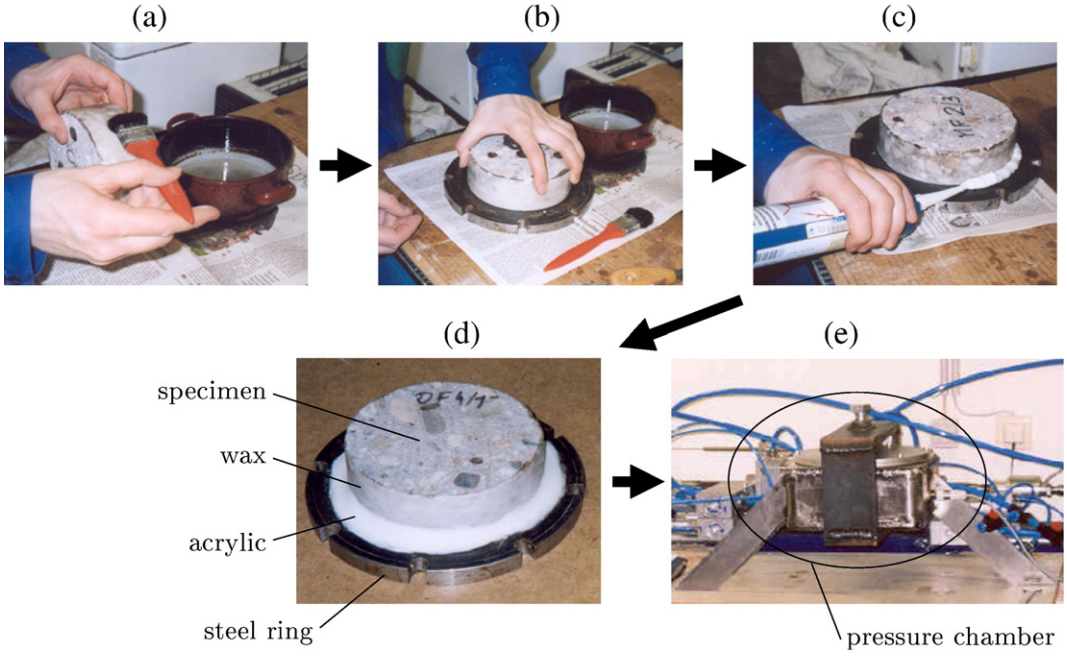


Fig. 16. Specimen preparation: (a) sealing of lateral surface, (b) placement of specimen in steel ring, (c) sealing of gap, (d) specimen plus steel ring before placement in pressure chamber, (e) pressure chamber containing permeability specimen.

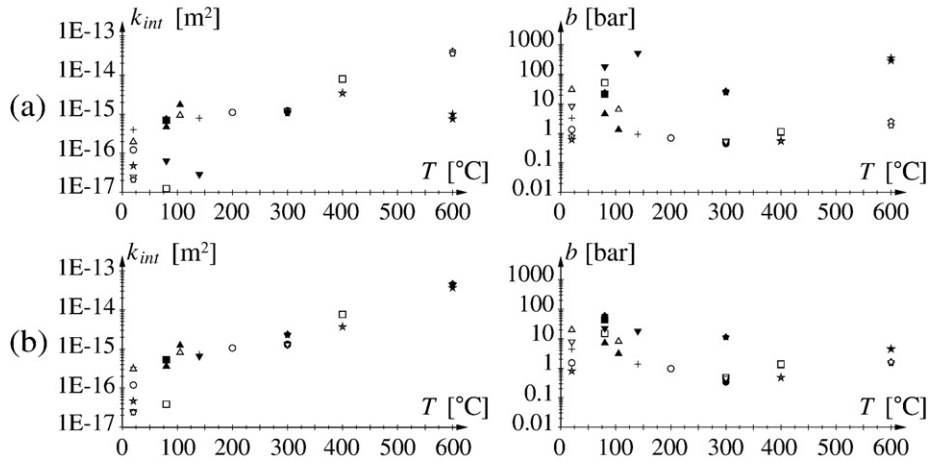


Fig. 17. $k_{int}$ and $b$ obtained from DPE as a function of temperature for in-situ concrete with 0 kg/m$^3$ PP-fibers and different modes of parameter identification: (a) stationary and (b) transient analysis (each symbol refers to one specimen which was tested at different temperatures).

temperatures of 200–300 °C, $b$ decreases for increasing pre-heating temperature. Thereafter it shows an increasing behavior. Comparing the different modes of parameter identification using results from DPE, the earlier (for in-situ concrete) observed deviation introduced by the assumption of stationary conditions is less pronounced. For this test series, the scatter of the identified parameters is larger when using experimental data from CPE (see Figs. 20 and 22), which is explained by the larger number of CPE performed.

## 5. Discussion

### 5.1. Stationary versus transient analysis for parameter identification

The stationary analysis provides several permeability values $k$ for different time intervals of the pressure history, giving access to $k_{int}$ and $b$ by linear approximation of the obtained permeability values and extrapolation towards $1/p=0$ (see Fig. 23). Since both DPE and CPE are conducted at pressures $p<10$ bar, the variation of the permeability values $k$ gives different possibilities for $k_{int}$ and $b$, as illustrated in Fig. 23. Therefore, the parameters identified from stationary analysis provide the correct permeability $k$ (with $k=k_{int}(1+b/p)$) in the pressure range considered in the experiment. Nevertheless, the identified values for $k_{int}$ and $b$ might show considerable scatter, especially in case of DPE (see, e.g., Figs. 17(a) and 18(a)). The scatter of the experimental results may be reduced by increasing the pressure range considered in the experiments, which would result in $k$-values closer to $1/p=0$. In this case, however, the pressurized volume must be increased in order to avoid transient effects at higher pressures as indicated in Fig. 23. On the other hand, the increase of the pressurized volume results in an increased scatter at low pressures when the pressure decrease approaches the accuracy range of the pressure gauge. Figs. 20(a) and 22(a) show that the scatter of the identified parameters from the stationary analysis is considerably smaller for CPE compared to the parameters obtained from the DPE. This is explained by the almost constant pressure in the pressurized volume (see Fig. 9). Thus, no pressure deviations alter the experimental results of the CPE and stationary conditions are guaranteed.

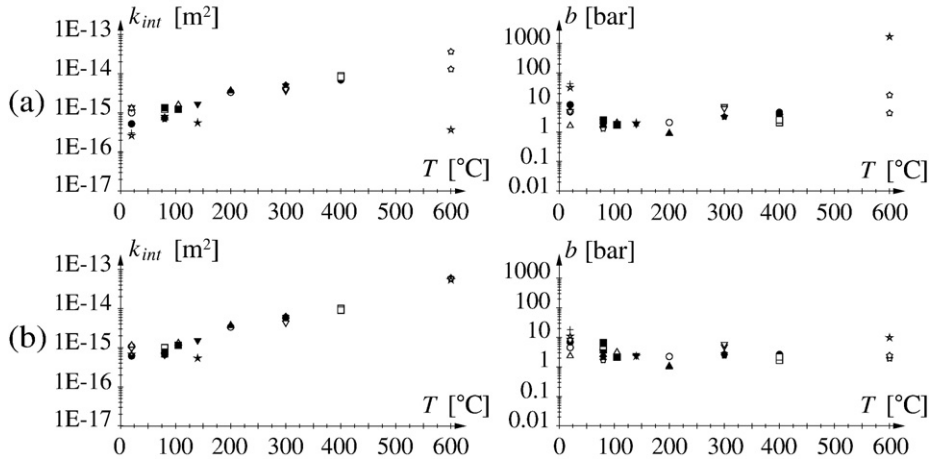


Fig. 18. $k_{int}$ and $b$ obtained from DPE as a function of temperature for in-situ concrete with 1.5 kg/m$^3$ PP-fibers and different modes of parameter identification: (a) stationary and (b) transient analysis (each symbol refers to one specimen which was tested at different temperatures).

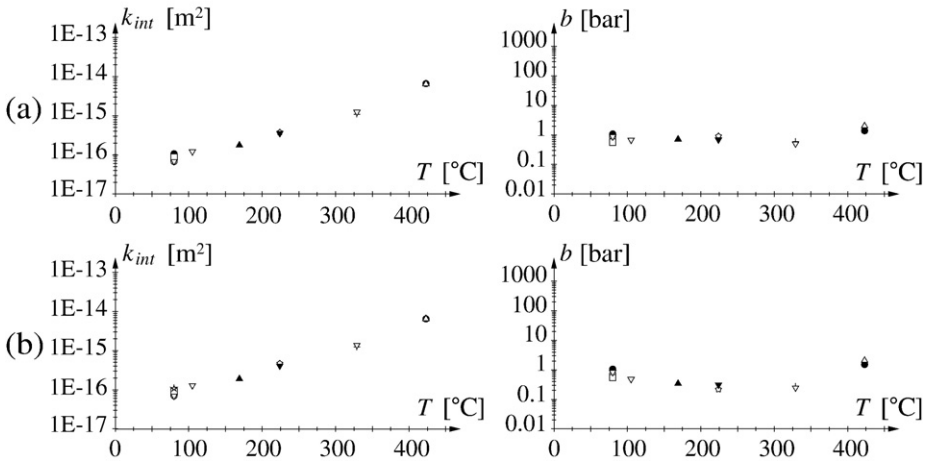


Fig. 19. $k_{int}$ and $b$ obtained from DPE as a function of temperature for laboratory-cast concrete with 0 kg/m$^3$ PP-fibers and different modes of parameter identification: (a) stationary and (b) transient analysis (each symbol refers to one specimen which was tested at different temperatures).

Compared to the stationary analysis, the transient analysis leads to less scatter for the permeability parameters identified from DPE (see, e.g., Figs. 17(b) and 18(b)), which is explained by capturing transient effects when solving the one-dimensional mass-balance equation for the gas phase (see Eq. (18)). Fig. 24(a) shows the error between the numerically and experimentally-obtained pressure decrease for different values of $k_{int}$ and $b$. Whereas the result identified from stationary analysis is located in the "valley" characterized by a lower error, the result of the transient analysis coincides with the global minimum of $R$ (see Fig. 24). The error between the numerically and experimentally-obtained pressure history is illustrated in Fig. 25, showing $p_t(t)$ obtained from the transient analysis (i.e., $p_t^{num}(t)$) related to the respective experimental pressure history (i.e., $p_t^{exp}(t)$). As already indicated in Fig. 24, the permeability parameters from the transient analysis give better agreement between the computed and measured pressure history obtained during DPE.

### 5.2. Are both $k_{int}$ and $b$ required to define gas-transport properties of concrete?

Figs. 23 and 24 highlight the fact that different ($k_{int}$,$b$)-pairs give similar permeability values $k$ measured during both DPE and CPE. In case of the stationary analysis, the same range of permeability values may be obtained in the pressure range the permeability experiment was performed using significantly different values for the intrinsic permeability $k_{int}$ and the slip-flow constant b (see Fig. 23). As indicated in Fig. 24, $k_{int}$ might vary over several orders of magnitude. Hereby, an increase of $k_{int}$ is accompanied by a decrease of $b$ until a certain value of $k_{int}$ is reached. Thereafter, the "valley" observed in Fig. 24 turns and $k_{int}$ becomes independent of $b$, indicating pressure-independence for the permeability. As a consequence, the identification of $k_{int}$ from gas-permeability tests is not unique. In fact, an infinite number of ($k_{int}$,$b$)-pairs would give proper permeability values in the pressure range considered in the experiment. Thus, both $k_{int}$ *and* $b$ must be provided in order to properly define the gas-transport properties of concrete. Among the different possibilities, the ($k_{int}$,$b$)-pair representing the measured $k$-values best corresponds to the global minimum of the error encountered in the aforementioned "valley".

### 5.3. Influence of PP-fibers and the production process on the permeability

In this subsection, differences (i) between concrete with and without PP-fibers and (ii) between in-situ and laboratory-cast concrete are highlighted. Comparing the results for in-situ concrete with and without PP-fibers (see Figs. 26 and 27), the following differences within certain temperature ranges are observed:

(1) At room temperature (20 °C), a big difference in $k_{int}$ is observed (see Fig. 26(a)), whereas $b$ is practically the same for concrete with and without PP-fibers (see Fig. 26(b)). Thus, the permeability $k$ (with $k=k_{int}(1+b/p)$, see Eq. (3)) has the same difference as $k_{int}$ (see Fig. 27).

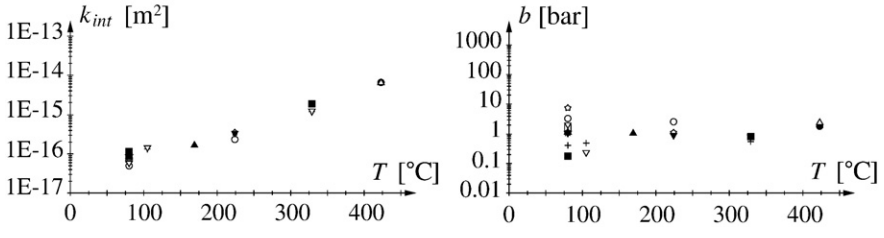


Fig. 20. $k_{int}$ and $b$ obtained from CPE as a function of temperature for laboratory-cast concrete with 0 kg/m$^3$ PP-fibers (stationary analysis, each symbol refers to one specimen which was tested at different temperatures).

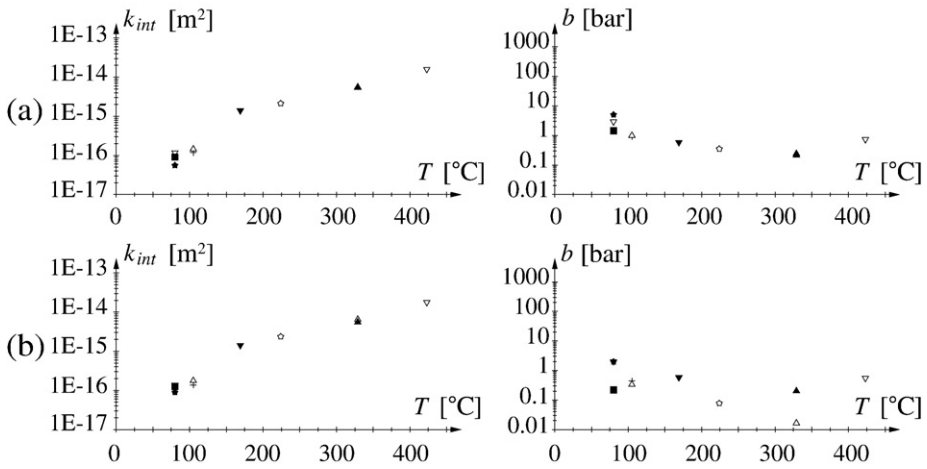


Fig. 21. $k_{int}$ and $b$ obtained from DPE as a function of temperature for laboratory-cast concrete with 1.5 kg/m$^3$ PP-fibers and different modes of parameter identification: (a) stationary and (b) transient analysis (each symbol refers to one specimen which was tested at different temperatures).

(2) For a pre-heating temperature of 80 °C, the difference of $k_{int}$ between concrete with and without PP-fibers decreases, whereas the opposite is the case for $b$ ($b$ increases considerably for concrete without PP-fibers and it decreases for concrete with fibers, causing an increase of the difference in $b$). Consequently, the permeability $k$ increases in case of concrete without PP-fibers, whereas a decrease in case of concrete with fibers is observed (see Fig. 27). The observed behavior of the permeability $k$ illustrates the importance of considering both permeability parameters ($k_{int}$ and $b$) to represent the gas permeability of concrete.

(3) For temperatures between 80 and 140 °C, an oscillating behavior of the permeability parameters is observed with opposite trends for $k_{int}$ and $b$ (see Fig. 26), giving almost constant values for $k$ within this temperature range.

(4) For pre-heating temperatures between 140 and 200 °C, the difference in $k_{int}$ between in-situ concrete with and without PP-fibers increases considerably, reaching the same magnitude as observed for the low-temperature permeabilities (for $T$=20 °C). The difference in $b$ decreases, yielding an increase of the difference in $k$ (see Fig. 27). This increase is explained by melting of the PP-fibers. In contrast to the results obtained for laboratory-cast concrete [15], showing the maximum difference at a pre-heating temperature of 200 °C, this "fiber effect" was at the most of equal importance as the aforementioned difference in low-temperature permeability, with the latter considered to be mainly affected by the construction process of the concrete members.

(5) Above 200 °C, the difference in $k_{int}$ decreases again whereas the difference in $b$ between concrete with and without PP-fibers remains almost constant. This leads to a decreasing difference of the permeability $k$ (see Fig. 27), indicating that temperature-induced damage overshadows the effect of melting of the PP-fibers on the permeability.

Comparing laboratory-cast concrete with and without PP-fibers (Figs. 28 and 29), the following observations are made:

(1) In contrast to in-situ concrete, laboratory-cast concrete shows no distinct difference in low-temperature permeabilities between concrete with and without fibers. Up to a pre-heating temperature of 105 °C, the intrinsic permeability $k_{int}$ is practically the same (see Fig. 28(a)). As regards the value of $b$, only small differences are observed, yielding almost equal values for the permeability $k$ for concrete with and without PP-fibers (see Fig. 29). This is in agreement with experimental results obtained for laboratory-cast concrete presented in [15].

(2) The observed "fiber effect" is also found in laboratory-cast concrete with 1.5 kg/m$^3$ PP-fibers. Whereas $k_{int}$ increases continuously in case of concrete without PP-fibers between pre-heating temperatures of 105 and 170 °C, a jump of almost one order of magnitude is

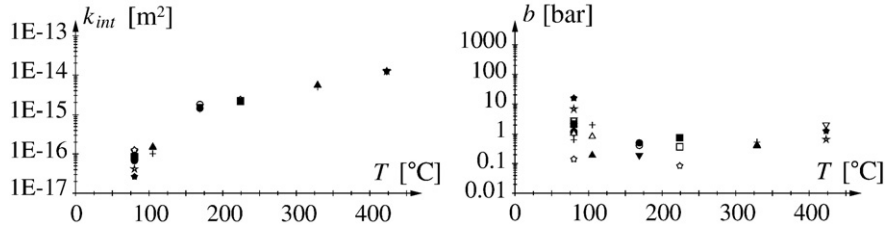


Fig. 22. $k_{int}$ and $b$ obtained from CPE as a function of temperature for laboratory-cast concrete with 1.5 kg/m$^3$ PP-fibers (stationary analysis, each symbol refers to one specimen which was tested at different temperatures).

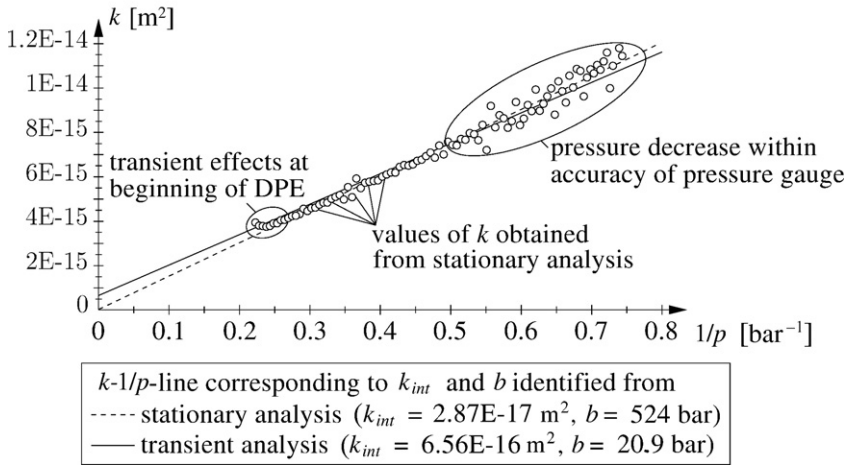


Fig. 23. Parameter identification for selected DPE using stationary analysis (comparison with result from respective transient analysis).

observed for $k_{int}$ of concrete with fibers. The slip-flow constant $b$, on the other hand, shows no jump. In case of concrete with PP-fibers, $b$ decreases and becomes lower than the value of $b$ of concrete without fibers. The observed changes in $k_{int}$ and $b$ lead to a sudden increase of the difference of the permeability $k$ (see Fig. 29) which is considered to be caused by melting of the fibers, as in case of in-situ concrete.

(3) For pre-heating temperatures above 170 °C, the difference in $k_{int}$ between concrete with and without PP-fibers decreases as observed in case of in-situ concrete. The difference in $b$ remains almost constant, yielding a

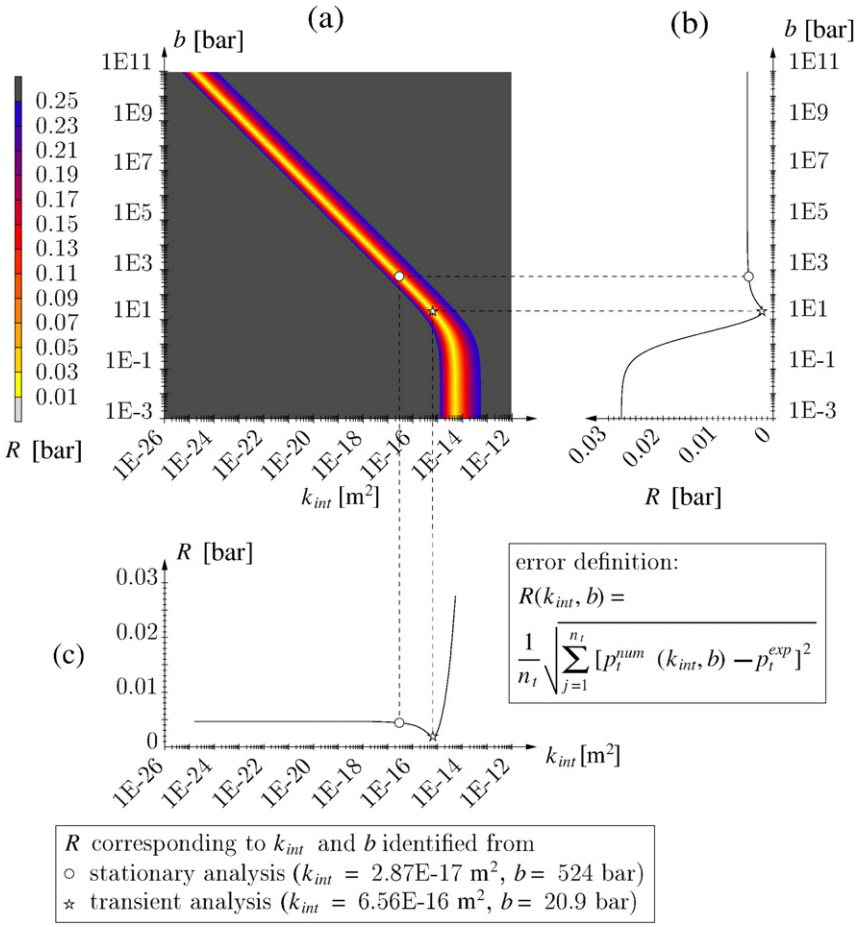


Fig. 24. Results from transient analysis of selected DPE: (a) distribution of error $R$ as a function of $k_{int}$ and $b$; plot of error "valley" as a function of (b) $b$ and (c) $k_{int}$ ($n_t$: number of time instants considered during minimization of $R$; $p_t^{num}$: numerical pressure history; $p_t^{exp}$: measured pressure history).

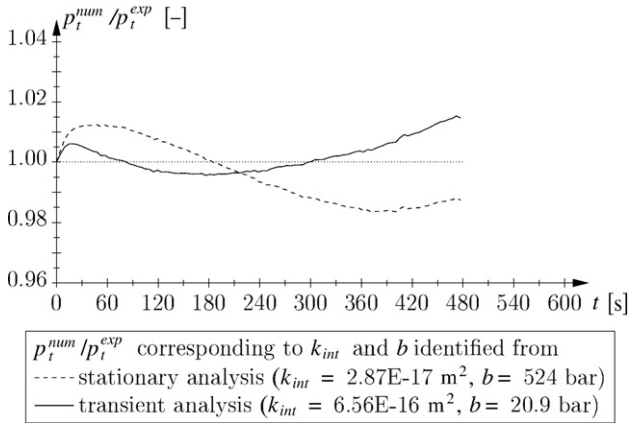


Fig. 25. Ratio $p_t^{num}/p_t^{exp}$ for two ($k_{int}$,$b$)-pairs during transient analysis of selected DPE.

continuous decrease of the difference in $k$. This indicates again that temperature-induced damage overshadows the effect of melting of the PP-fibers.

The differences between concrete with and without PP-fibers may be explained by:

- For low temperatures, this difference was only observed in case of in-situ concrete, whereas similar permeability parameters were observed for laboratory-cast concrete. Based on mercury-intrusion-porosimetry (MIP) test results, the observed difference was assigned to the considerably higher pore volume for in-situ concrete containing PP-fibers. This higher amount of pore volume was encountered in the pore-size range corresponding to the thickness of the interfacial transition zones (ITZ) [2], which is in agreement with theories presented in [1,26,27], stating that the PP-fibers introduce additional ITZ at casting. As found by means of numerical simulations of the formation of the concrete microstructure [26], the introduction of additional ITZ by PP-fibers connects locally-percolated ITZ clusters, leading to percolation of the overall pore structure. The effect of PP-fibers on the low-temperature permeability, which was found only for in-situ concrete, is explained by the reduced on-site workability and the lower effect of densification of concrete containing PP-fibers [1], eventually influencing the pore structure of the in-situ concrete and/or the characteristics of the ITZ [2]. Moreover, internal bleeding in consequence of a higher amount of liquefier influences the formation of ITZ [1].

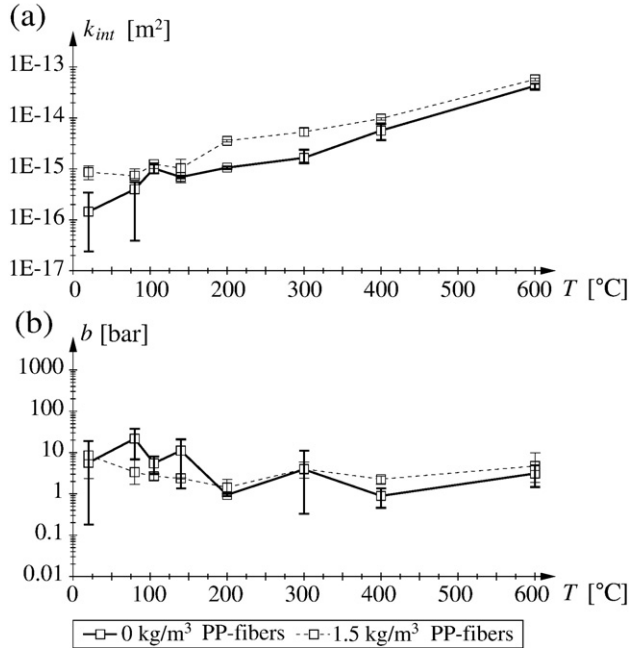


Fig. 26. Permeability parameters $k_{int}$ and b for in-situ concrete with 0 and 1.5 kg/m³ PP-fibers (values taken from DPE/transient analysis, see Figs. 17(b) and 18(b); squares represent average values, lines mark minimum and maximum value).

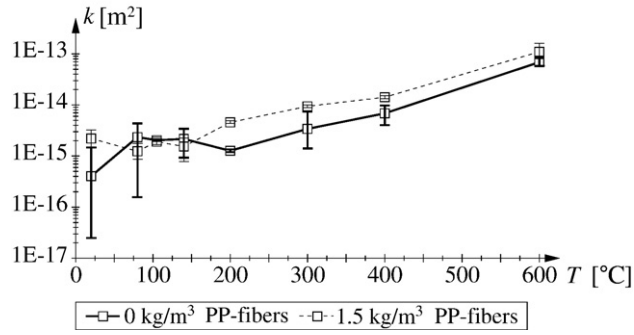


Fig. 27. Permeability $k$ at $p$=5 bar (with $k=k_{int}(1+b/p)$) for in-situ concrete with 0 and 1.5 kg/m3 PP-fibers ($k_{int}$ and $b$ identified from DPE/transient analysis, see Figs. 17(b) and 18(b); squares represent average values, lines mark minimum and maximum value).

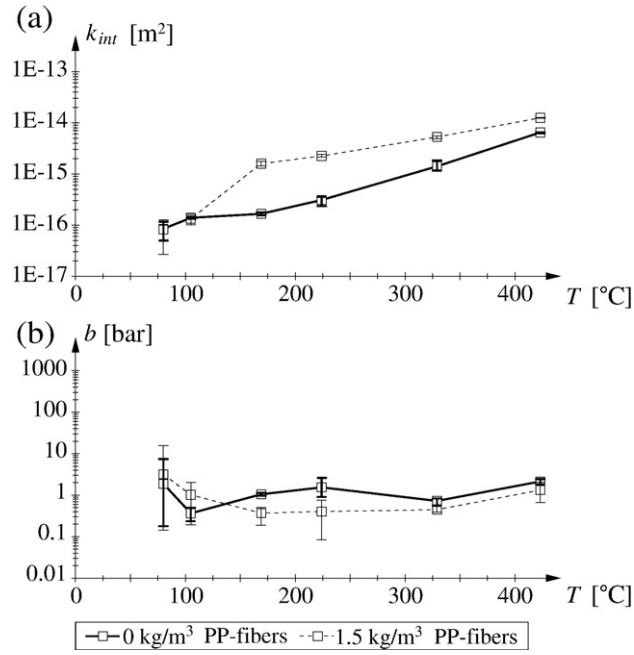


Fig. 28. Permeability parameters $k_{int}$ and $b$ for laboratory-cast concrete with 0 and 1.5 kg/m³ PP-fibers (values taken from CPE/stationary analysis, see Figs. 20 and 22; squares represent average values, lines mark minimum and maximum value).

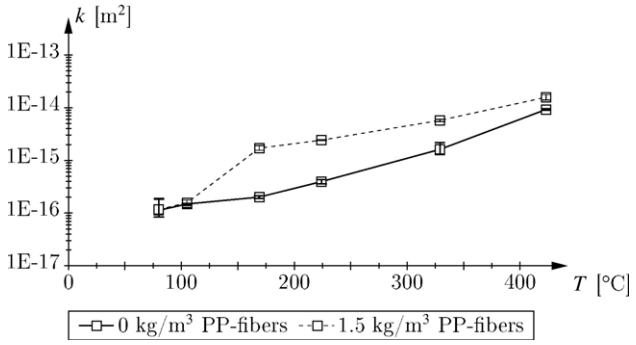


Fig. 29. Permeability $k$ at $p=5$ bar (with $k=k_{int}(1+b/p)$) for laboratory-cast concrete with 0 and 1.5 kg/m$^3$ PP-fibers ($k_{int}$ and b identified from CPE/stationary analysis, see Figs. 20 and 22; squares represent average values, lines mark minimum and maximum value).

- The sharp increase of the permeability of concrete with PP-fibers at a temperature of $T\approx 170$ °C was observed for in-situ as well as laboratory-cast concrete. According to [15], this permeability jump is caused by melting of the polypropylene fibers followed by the partial or complete absorption of the molten polypropylene by the cement matrix [15], leaving additional pathways for gas to flow through the porous matrix. In addition, the different microcracking behavior could have an influence on the considerably different permeability. Experiments [15] revealed a much higher crack density in case fiber-reinforced concrete was heated to temperatures above 170 °C compared to concrete without fibers, whereas larger crack widths were observed for the latter. This difference in cracking behavior might be caused by (i) the fibers acting as discontinuities within the cement matrix and therefore favoring nucleation of local cracks [15] and (ii) the expansion of polypropylene during melting [15,28]. As regards the latter, the crystalline part of polypropylene (amounting to 60 vol.-% of the employed polypropylene) is transformed into amorphous polypropylene, with the overall density dropping from 910 kg/m$^3$ to 850 kg/m$^3$ [24], giving an increase in volume of approximately 7%. In any case, the better-developed network in case of fiber-reinforced concrete increases the permeability via a higher number of pathways for the vapor to move towards the heated surface.

## 6. Conclusions and outlook

In this paper, different modes for identification of the permeability parameters of porous media, i.e., the intrinsic permeability $k_{int}$ and the so-called slip-flow constant $b$, were proposed, employing (i) constant pressure experiments (CPE, stationary conditions) and (ii) decreasing pressure experiments (DPE, transient conditions). As regards the latter, transient effects, reflected by similar time scales for changes of gas pressure applied onto the specimen and the gas flow through the specimen, were well captured, leading to a reduction of the scatter of the identified permeability parameters $k_{int}$ and $b$. Even though stationary as well as transient analyses have shown that different ($k_{int}$,$b$)-pairs represent the experimentally-obtained permeability values with similar accuracy, the presented transient analysis gave the ($k_{int}$,$b$)-pair corresponding to the global minimum of the error between numerically and experimentally-obtained decrease of the applied pressure in DPE. In case of CPE, the almost-constant pressure in the pressurized volume justified application of the stationary analysis.

The proposed tool was used for identification of residual gas-transport properties of in-situ as well as laboratory-cast concrete with/without polypropylene (PP) fibers subjected to elevated temperatures, revealing the following:

- For low temperatures, a difference between concrete with and without PP-fibers was observed in case of in-situ concrete, whereas similar permeability parameters were observed for laboratory-cast concrete. This difference may be attributed to the introduction of additional interfacial transition zones (ITZ) at casting. Since this difference in low-temperature permeabilities was only observed for in-situ concrete, on-site effects such as the reduced workability and the lower effect of densification of concrete containing PP-fibers might influence the pore structure of the in-situ concrete and/or the characteristics of the ITZ.
- The permeability jump in case of concrete including PP-fibers was observed at the melting temperature of polypropylene for in-situ as well as laboratory-cast concrete. This permeability increase may be explained by (i) melting of polypropylene followed by its partial absorption by the surrounding cement matrix providing additional pore space and (ii) a different microcracking behavior of concrete with PP-fibers with the fibers acting as discontinuities and/or introducing additional microcracks in consequence of expansion of polypropylene during melting.

The observed differences in permeability are considered to originate from temperature-dependent changes of specific characteristics of the material microstructure, with the latter requiring further experimental investigation in order to verify the underlying mechanisms (e.g., introduction of additional ITZ by PP-fibers and the corresponding percolation threshold, different microcracking behavior of concrete containing fibers). In addition to that, future work is devoted to linking changes in the material microstructure to changes of macroscopic material parameters by means of multiscale models (considering, e.g., the structural scale, the aggregate scale, and the cement-paste scale). This link is established by appropriate upscaling/homogenization techniques, which are validated by experiments at the different scales.

## Acknowledgments

The authors are grateful to Wolfgang Kusterle, University of Applied Sciences (Regensburg, Germany) for the fruitful cooperation within the research project “Fire Resistance of Fiber-reinforced, Reinforced, and Prestressed Concrete” (“Brandbeständigkeit von Faser-, Stahl-und Spannbeton”, sponsored by the Austrian Ministry for Transportation and the ÖEBB-Infrastruktur Bau AG, Vienna, Austria), to Ulrich Schneider and Hadubrand Harand from the Center for Material Research, Testing and Fire Safety Science at Vienna University of Technology (Vienna, Austria) for cooperation during preparing the laboratory-cast

specimens, and to Georg Ferner for assistance during permeability testing of the laboratory-cast specimens. Moreover, they wish to thank Christian Schmid and Wolfgang Dörner from the Institute for Mechanics of Materials and Structures at Vienna University of Technology (Vienna, Austria) and Alfred Leithner from Donau Chemie AG, Pischelsdorf for assistance during the design of the permeability measurement device. Assistance of Christian Zaruba from the Institute of Materials Science and Technology at Vienna University of Technology (Vienna, Austria) in the preparation of SEM-images of the polypropylene fibers as well as valuable information on the polypropylene fibers from Ann Lambrechts (NV Bekaert SA, Zwevegem, Belgium) are gratefully acknowledged. This research was conducted with financial support by the Austrian Science Fund (FWF) via project P16517-N07 "Transport processes in concrete at high temperatures".

## Appendix A. Numerical analysis of one-dimensional transient gas flow through the concrete specimen

According to [29], the macroscopic mass balance equation of the gas phase in porous media reads for the one-dimensional case[3]

$$-n\rho^{g}\frac{\partial S_{w}}{\partial t}+n(1-S_{w})\left(\frac{\partial \rho^{ga}}{\partial t}+\frac{\partial \rho^{gw}}{\partial t}\right)-\frac{\partial}{\partial x}\left(\rho^{g}\frac{kk^{rg}}{\eta}\frac{\partial p^{g}}{\partial x}\right)=0, \tag{A.1}$$

where $\rho^{ga}$ and $\rho^{gw}$ [kg/m$^3$] are the densities of dry air and water vapor, respectively, and $\rho^{g}$ [kg/m$^3$] is the gas (mixture of dry air and water vapor) density with $\rho^{g}=\rho^{ga}+\rho^{gw}$. In Equation (A.1), $n$ [−] is the porosity of concrete, $S_w$ [−] is the water saturation, $k^{rg}$ [−] is the relative permeability of concrete to gas flow, and $p^{g}$ [Pa] is the gas pressure. Assuming that no water is present within the concrete specimen gives $S_w=0$ and $k^{rg}=1$. Therefore, Equation (A.1) reduces to

$$n\left(\frac{\partial \rho^{ga}}{\partial t}+\frac{\partial \rho^{gw}}{\partial t}\right)-\frac{\partial}{\partial x}\left(\rho^{g}\frac{k}{\eta}\frac{\partial p^{g}}{\partial x}\right)=0. \tag{A.2}$$

Note that the third term in Eq. (A.2) contains Darcy's law for pressure-driven flow, reading $v=-k/\eta\cdot\partial p^{g}/\partial x$, with $v$ [m/s] as the velocity of the advected gas (compare to Eq. (1) in Section 2.2, with $Q=A\cdot v$). Since the permeability experiments were performed at room temperature at which vapor transport may be neglected, $\rho^{gw}=0$ yields $\rho^{g}=\rho^{ga}$ and $p^{g}=p^{ga}=p$. Inserting Eq. (3) into Eq. (A.2) and considering Clapeyron's law for ideal gases, giving $\rho^{ga}=M_a/(RT)\cdot p$, with $M_a=0.029$ kg/mol as the molar mass of air, $R=8.31$ J/(mol K) as the gas constant, and $T$ [K] as the constant temperature, leads to (after division by $M_a/(RT)$)

$$n\frac{\partial p}{\partial t}-\frac{k_{int}}{\eta}\frac{\partial}{\partial x}\left[(p+b)\frac{\partial p}{\partial x}\right]=0. \tag{A.3}$$

[3] In contrast to [29], neither movement of the solid phase nor mass sources/sinks are considered. Moreover, the temperature is assumed to be constant (therefore, the respective time derivative vanishes).

## B. Alternative determination of $k_{int}$ and $b$ by iterative analysis

Alternatively to the determination of $k_{int}$ and $b$ by linear regression as illustrated in Fig. 6, an iterative numerical scheme (as described in [30] and used in [2]) may be employed. For this purpose, Eq. (2) is rearranged, giving

$$Q(x)p(x)=-k_{int}\frac{A}{\eta}\frac{dp}{dx}[p(x)+b]. \tag{B.1}$$

Within the iterative analysis, the (experimentally-obtained) pressure history is prescribed at the top surface of the specimen and the error in the pressure history at the bottom surface is minimized, assuming stationary flow through the specimen for the different time intervals $t_1\le t\le t_2$. Because of the use of different definitions for the error (least-square error in regression analysis and error in pressure history at the bottom surface of the specimen in iterative numerical scheme), the iterative scheme proofed to be more stable in case of DPE (for CPE, no distinct differences were observed). However, as shown in Section 2.2.2, the assumption of stationary flow within the different time intervals is questionable in case of DPE. For determination of the permeability parameters from CPE, the more simple regression analysis is used.

## C. Back-calculation of material parameters for in-situ concrete

Considering the recorded mixing parameters of in-situ concrete without PP-fibers and $f_i=m_i/\rho_i$, with $i\in\{$agg… aggregates, cem… cement, fa…. fly ash, w… water, a… air$\}$, where $f_i$ [−] and $m_i$ [kg/m$^3$] are the specific volume fraction and the mass of the respective constituent per m$^3$ of fresh concrete and $\rho_i$ [kg/m$^3$] is the respective specific density, yields the volume fraction of aggregates as

$$\begin{aligned} f_{agg} &= 1-f_a-f_w-f_{fa}-f_{cem}\\ &= 1-0.035-\frac{157}{1000}-\frac{60}{2300}-\frac{260}{3150}=0.70 \end{aligned} \tag{C.1}$$

This leads to the specific aggregate density as

$$\rho_{agg}=\frac{m_{agg}}{f_{agg}}=\frac{1909}{0.70}=2730\ \text{kg/m}^3. \tag{C.2}$$

In case of in-situ concrete with 1.5 kg/m$^3$ PP-fibers, the aggregate mass can be determined from the concrete density as

$$\begin{aligned} \rho &= m_{agg}+m_{cem}+m_{fa}+m_w+m_{PP}\\ &= 2352\,\text{kg/m}^3\rightarrow\\ m_{agg} &= \rho-m_{PP}-m_w-m_{fa}-m_{cem}\\ &= 2352-1.5-157-60-260=1873.5\,\text{kg/m}^3, \end{aligned} \tag{C.3}$$

where $m_{PP}=1.5$ kg/m$^3$ is the mass of the PP-fibers. With all specific densities at hand, the air content of in-situ concrete with

1.5 kg/m$^3$ PP-fibers can be determined from

$$f_a = 1 - f_{PP} - f_w - f_{fa} - f_{cem} - f_{agg} = 1 - \frac{1.5}{910} - \frac{157}{1000} - \frac{60}{2300} - \frac{260}{3150} - \frac{1873.5}{2730} = 0.046. \quad (C.4)$$

## References


[1] W. Kusterle, W. Lindlbauer, G. Hampejs, A. Heel, P.-F. Donauer, M. Zeiml, W. Brunnsteiner, R. Dietze, W. Hermann, H. Viechtbauer, M. Schreiner, R. Vierthaler, H. Stadlober, H. Winter, J. Lemmerer, E. Kammeringer, Brandbeständigkeit von Faser-, Stahl- und Spannbeton [Fire resistance of fiber-reinforced, reinforced, and prestressed concrete], Bundesministerium für Verkehr, Innovation und Technologie, Vienna, in German, Tech. Rep., vol. 544, 2004.

[2] M. Zeiml, D. Leithner, R. Lackner, H.A. Mang, How do polypropylene fibers improve the spalling behavior of in-situ concrete? Cement and Concrete Research 36 (5) (2006) 929–942.

[3] J.W. Figg, Methods of measuring the air and water permeability of concrete, Magazine of Concrete Research 25 (85) (1973) 213–219.

[4] P.A. Claisse, H.I. Elsayad, I.G. Shaaban, Test methods for measuring fluid transport in cover concrete, Journal of Materials in Civil Engineering 11 (2) (1999) 138–143.

[5] R.K. Dhir, P.C. Hewlett, Y.N. Chan, Near surface characteristics of concrete: assessment and development of in-situ test methods, Magazine of Concrete Research 39 (141) (1987) 183–195.

[6] P.B. Bamforth, The relationship between permeability coefficients for concrete obtained using liquid and gas, Magazine of Concrete Research 39 (138) (1987) 3–11.

[7] H. Loosveldt, Z. Lafhaj, F. Skoczylas, Experimental study of gas and liquid permeability of mortar, Cement and Concrete Research 32 (2002) 1357–1363.

[8] G.W. Scherer, Measuring permeability of rigid materials by a beam-bending method: I, theory, Journal of the American Ceramics Association 83 (9) (2000) 2231–2239.

[9] W. Vichit-Vadakan, G.W. Scherer, Measuring permeability of rigid materials by a beam-bending method: III, cement paste, Journal of the American Ceramics Association 85 (6) (2002) 1537–1544.

[10] G.W. Scherer, Dynamic pressurization method for measuring permeability and modulus: I. theory, Materials and Structures 39 (10) (2006) 1041–1057.

[11] Z.C. Grasley, G.W. Scherer, D.A. Lange, J.J. Valenza, Dynamic pressurization method for measuring permeability and modulus: II. cementitious materials, Materials and Structures 40 (7) (2007) 711–721.

[12] R. Cather, J.W. Figg, A.F. Marsden, T. O'Brien, Improvements to the Figg method for determining the air permeability of concrete, Magazine of Concrete Research 36 (129) (1984) 241–245.

[13] R.K. Dhir, P.C. Hewlett, E.A. Byars, I.G. Shaaban, A new technique for measuring the air permeability of near-surface concrete, Magazine of Concrete Research 47 (171) (1995) 167–176.

[14] J.J. Kollek, The determination of the permeability of concrete to oxygen by the CEM-Bureau method — a recommendation, Materials and Structures 22 (1989) 225–230.

[15] P. Kalifa, G. Chéné, C. Gallé, High temperature behaviour of HPC with polypropylene fibres: From spalling to microstructure, Cement and Concrete Research 31 (2001) 1487–1499.

[16] J.P. Monlouis-Bonnaire, J. Verdier, B. Perrin, Prediction of the relative permeability to gas flow of cement-based materials, Cement and Concrete Research 34 (5) (2004) 737–744.

[17] C. Gallé, J.-F. Daian, Gas permeability of unsaturated cement-based materials: application of a multi-scale network model, Magazine of Concrete Research 52 (4) (2000) 251–263.

[18] U. Schneider, H.J. Herbst, Permeabilität und Porosität von Beton bei hohen Temperaturen [Permeability and porosity of concrete at high temperatures], Deutscher Ausschuss für Stahlbeton, Berlin, in German, Tech. Rep., vol. 403, 1989.

[19] L.J. Klinkenberg, The permeability of porous media to liquids and gases, American Petroleum Institute, Drilling Production Practice (1941) 200–213.

[20] F.P. Jacobs, Permeabilität und Porengefüge zementgebundener Werkstoffe [Permeability and pore structure of cementitious materials], Ph.D. thesis, ETH Zürich, Zürich, Switzerland, in German (1994).

[21] F.D. Lydon, Effect of coarse aggregate and water/cement ratio on intrinsic permeability of concrete subject to drying, Cement and Concrete Research 25 (1995) 1737–1746.

[22] J.D. Logan, Transport modeling in hydrogeomechanical systems, Springer, New York, 2001.

[23] Österreichisches Normungsinstitut, ÖNORM B4200-10, Beton — Herstellung, Verwendung und Gütenachweis [Concrete — Production, use and verification of quality], in German (1996).

[24] N. Pasquini, Polypropylene handbook, 2nd Edition, Hanser Publishers, Munich, 2005.

[25] A. Lambrechts, NV Bekaert, Zwevegem, Belgium, Private communications (2006).

[26] D.P. Bentz, Fibers, percolation, and spalling of high-performance concrete, ACI Materials Journal 97 (3) (2000) 351–359.

[27] U. Schneider, J. Horvath, Abplatzverhalten an Tunnelinnenschalenbeton [Spalling of concrete for tunnel linings], Beton- und Stahlbetonbau 97 (4) (2002) 185–190 in German.

[28] U. Schneider, Center for Material Research, Testing and Fire Safety Science, Vienna University of Technology, Vienna, Austria, Private communications (2006).

[29] R. Lewis, B. Schrefler, The finite element method in the static and dynamic deformation and consolidation of porous media, 2nd Edition, John Wiley & Sons, Chichester, 1998.

[30] R. Lackner, M. Zeiml, D. Leithner, G. Ferner, J. Eberhardsteiner, H.A. Mang, Feuerlastinduziertes Abplatzverhalten von Beton in Hohlraumbauten [Spalling behavior of concrete in underground facilities caused by fire], Verlag der Österreichischen Akademie der Wissenschaften, Vienna, Tech. Rep., vol. 9, 2007.